Supporting Information

Electron-Deficient Sites on Boron-Doped Graphite Enable Air-Stable and Durable Red Phosphorus Anode for Lithium-Ion Batteries

*Chuang Ji, Qingfeng Zhou, Yingyi Yuan, Wei Chen, Tao Hou, Bote Zhao, Yexia Qin, and Xunhui Xiong**

Experimental Section

***Pretreatment of RP*:** Typically, 1 g of commercial RP (98.5%, Aladdin) was ball-milled (QM-3SP04 supplied by the company of Nanjing Nada Instrument Co. Ltd.) in deionized water at 500 rpm for 24 h with 30 g zirconia balls (5 mm in diameter). After filtration, RP was added to 5 wt.% sodium hydroxide solution with continuous stirring for 6 h to remove the surface oxide layer. Then, the products were collected by filtration and rinsed several times with deionized water and anhydrous ethanol. Finally, RP was dried in a vacuum oven at 60 °C for 12 h.

***Preparation of BG, RP-G and RP-BG*:** In a typical experiment, 0.6 g purified RP, 0.4 g graphite (99.95%, Macklin) and 0.02 g amorphous boron (99%, Macklin) were sealed in a stainless ball mill jar under argon (Ar) atmosphere. After that, the corresponding RP-BG hybrids were obtained using one-step ball milling at a rotation speed of 500 rpm for 24 h. For comparison, the BG and RP-G composites were prepared by the same conditions.

***Morphology and structural characterization*:** The morphology and structure images of the as-prepared samples were obtained by a Hitachi Limited SU-8010 Field-emission scanning electron microscope (SEM) and a JEOL JEM 2100F transmission electron microscopy (TEM). X-ray diffraction (XRD) patterns were measured on a Bruker D8 Advanced Powder Diffractometer with Cu Ka radiation (k = 1.5418 Å). Raman data were collected by a Horiba JobinYvon HR800 Raman spectrophotometer. Fourier-transform infrared spectroscopy (FTIR, Bruker VERTEX 70 & ALPHA) and X-ray photoelectron spectroscopy (XPS, Thermo Scientific K-Alpha Nexsa) were performed to examine the phase composition of the composites. The Four probe powder resistivity tester (ST2722-sd) was used to investigate electronic conductivity. UV–vis spectra were collected by PE lambda 750. A Brunauer Emmett-Teller method (BET Micromeritics ASAP 2020) at the liquid-nitrogen boiling point (77 K) was used to confirmed the specific surface area.

***Electrochemical measurements*:** The electrode was prepared through mixing active material (80 wt.%), acetylene black (10 wt.%) and polyvinylidene fluoride (PVDF, 10 wt.%)

dissolved in N-methyl-2pyrrolidone (NMP), and then the slurry was coated onto the copper foil. After drying for 12 h at 80 °C, the copper foil was cut into discs with a diameter of 13 mm. The loading mass of active material on every disc is about 1.8 mg cm^{-2}, which was further upgraded to 2.6 and 3.5 mg cm^{-2}. Finally, the 2032 coin-type cells were assembled in an argon-filled glove box with the electrolyte of 1 mol L^{-1} LiPF6 in EC/DEC (1:1, v/v) with the addition of 5 wt.% FEC. A battery test system (LAND CT2001A) was used to evaluate the electrochemical performance with a voltage window of 0.01-3.00 V (vs. Li^+/Li). Cyclic voltammetry (CV, 0.01-3.00 V) and electrochemical impedance spectroscopy (EIS, 0.1-100000 Hz) were studied by the electrochemical workstation (CHI660E, Chenhua, Shanghai).

***DFT calculations*:** All calculations in this study were performed with the Vienna ab initio Simulation Package (VASP) within the frame of density functional theory (DFT). The exchange-correlation interactions of electron were described via the generalized gradient approximation (GGA) with PBE functional, and the projector augmented wave (PAW) method was used to describe the interactions of electron and ion. The Monkhorst-Pack scheme with a 2×2×1 k-point mesh was used for the integration in the irreducible Brillouin zone. The kinetic energy cut-off of 650 eV was chosen for the plane wave expansion. The lattice parameters and ionic position were fully relaxed, and the total energy was converged within 10^{-5} eV per formula unit. The final forces on all ions are less than 0.05/Å. The migration paths and energy barriers of Li ions were obtained via the nudged elastic band (NEB) method.

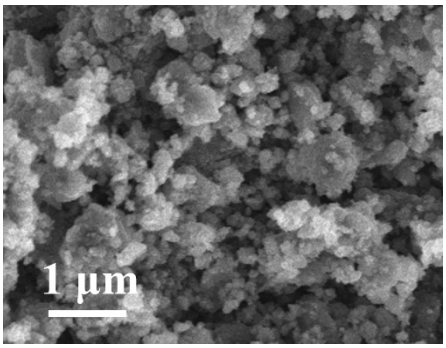

Figure S1. SEM images of RP-G.

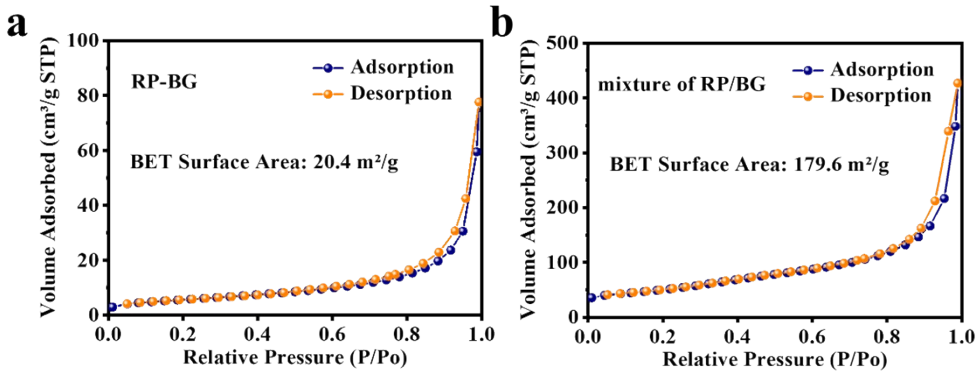

Figure S2. N_2 adsorption/desorption isotherms of (a) RP-BG and (b) mixture of RP/BG.

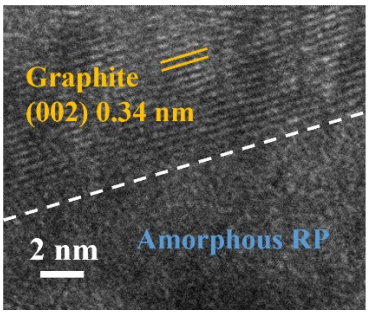

Figure S3. HRTEM images of RP-G.

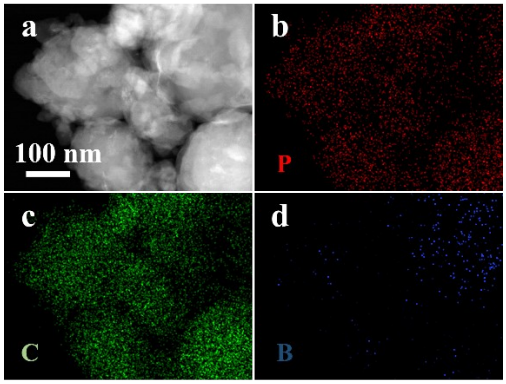

Figure S4. (a) STEM image of RP-BG and the corresponding elemental mapping images of (b) P, (c) C, and (d) B.

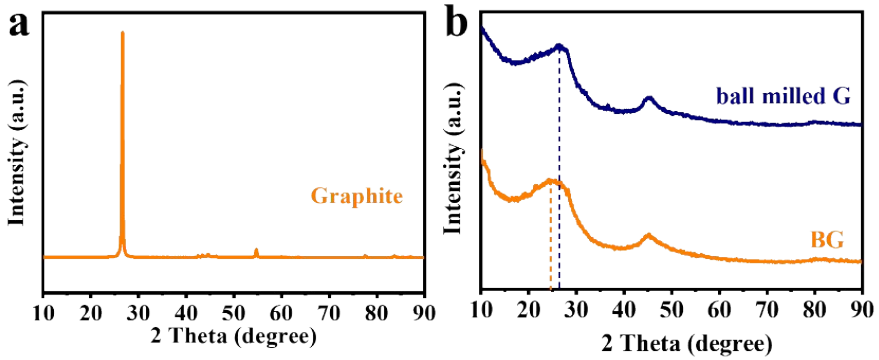

Figure S5. XRD patterns of (a) graphite; (b) ball milled G and BG.

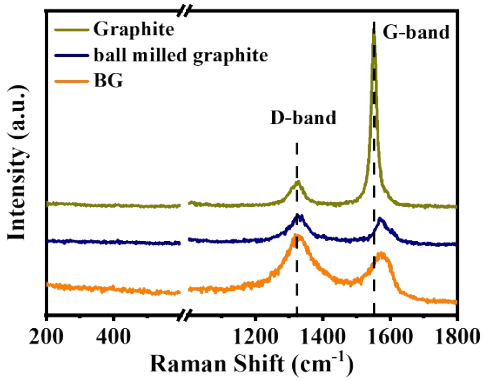

Figure S6. Raman spectra of graphite, ball milled graphite and BG.

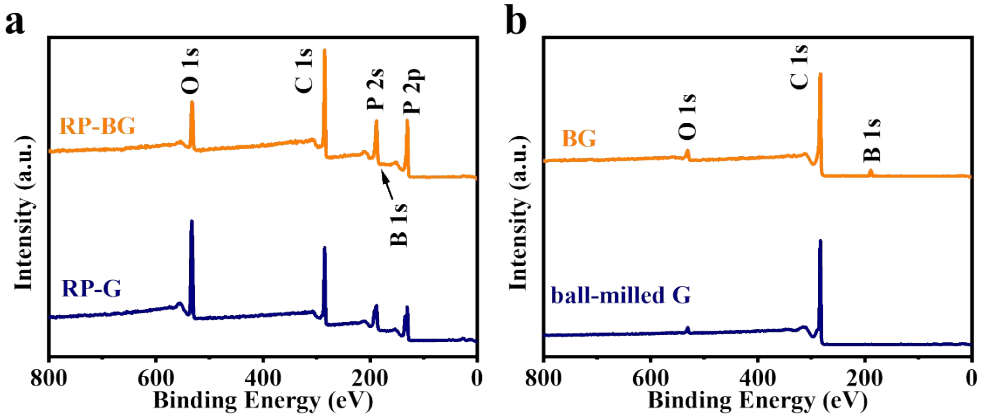

Figure S7. XPS survey spectra of (a) RP-G and RP-BG; (b) ball milled G and BG.

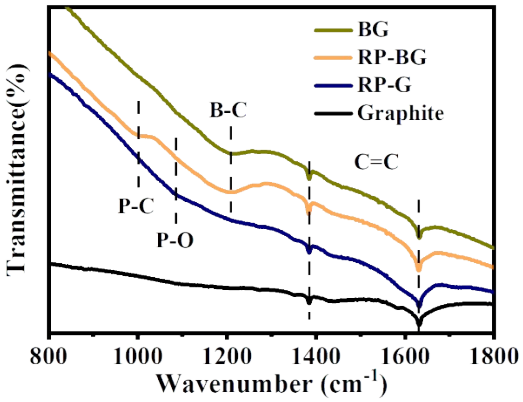

Figure S8. FTIR spectra of graphite, BG, RP-G and RP-BG.

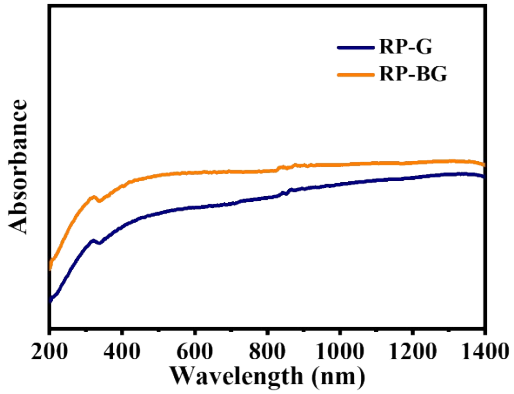

Figure S9. UV–vis spectra of RP-BG and RP-G.

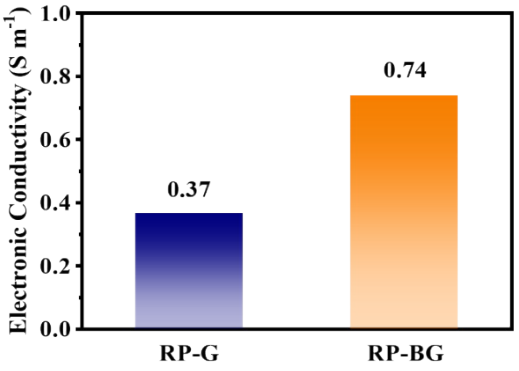

Figure S10. The electronic conductivities measured by four-probe method of RP-G and RP-BG at room temperature and normal pressure.

Table S1. Hall effect test results of ball milled graphite and BG

	Resistivity (Ω·cm)	Electronic mobility ($cm^2/V·S$)	Carrier density ($1/cm^3$)
BG	3.82×10^{-3}	12.70	1.29×10^{20}
ball milled graphite	1.21	5.84	8.81×10^{17}

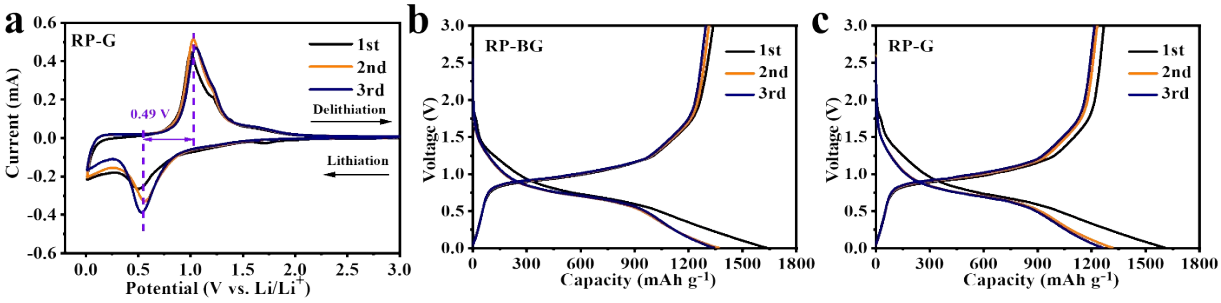

Figure S11. (a) CV curves of RP-G for the first three cycles at a scanning rate of 0.1 mV s^{-1}. Initial three galvanostatic charge-discharge profiles of (b) RP-BG and (c)RP-G at 0.1 A g^{-1}.

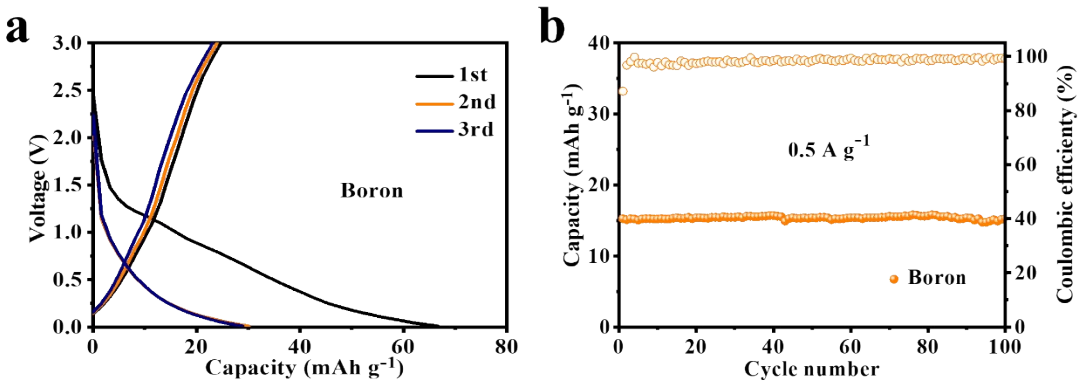

Figure S12. (a) Initial three galvanostatic charge-discharge profiles at 0.1 A g^{-1} and (b) cycle performance at 0.5 A g^{-1} of boron anode.

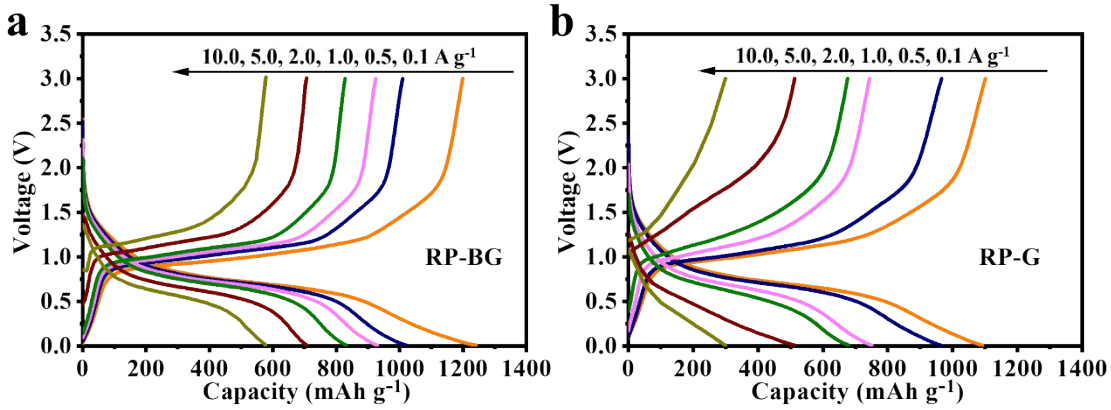

Figure S13. The charge-discharge profiles of (a) RP-BG and (b) RP-G at different current densities.

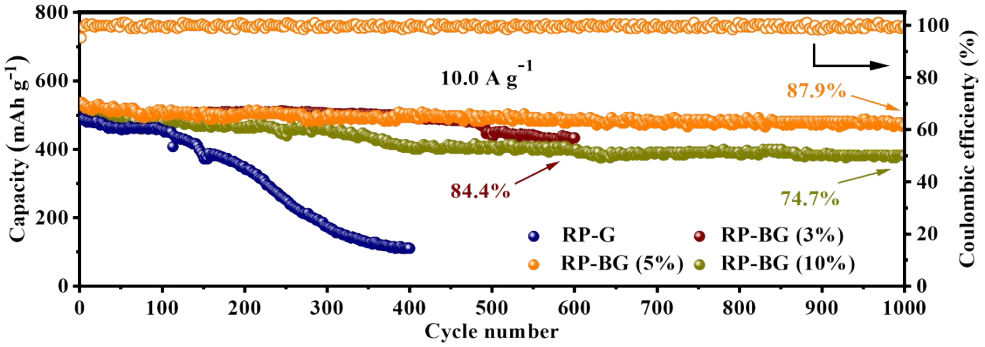

Figure S14. Cycling performance at 10.0 A g^{-1} of RP-BG with different boron doping levels.

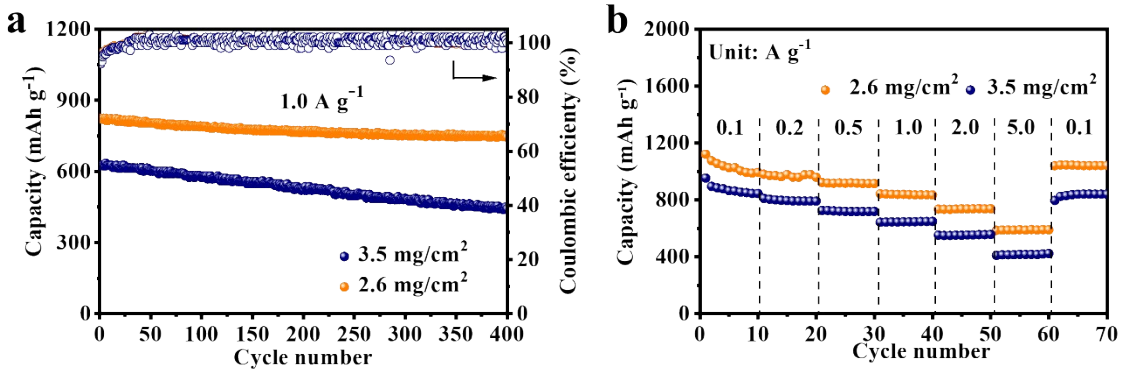

Figure S15. (a) Cycling performance at 1 A g^{-1} and (b) rate performance of RP-BG with different mass loading.

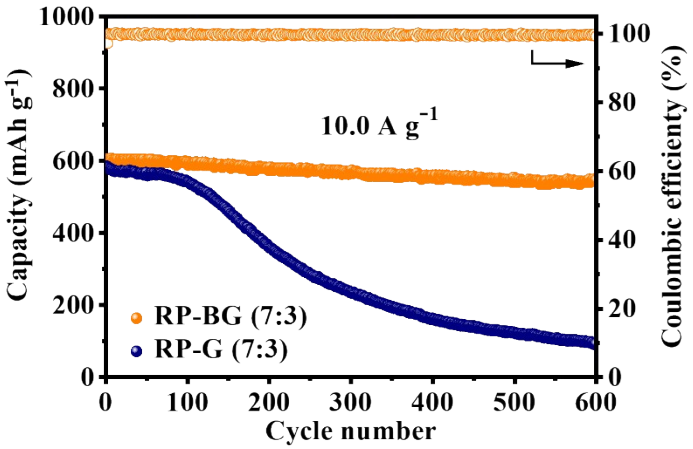

Figure S16. Cycling performance at 10.0 A g^{-1} of RP-BG with a mass ratio of 7:3.

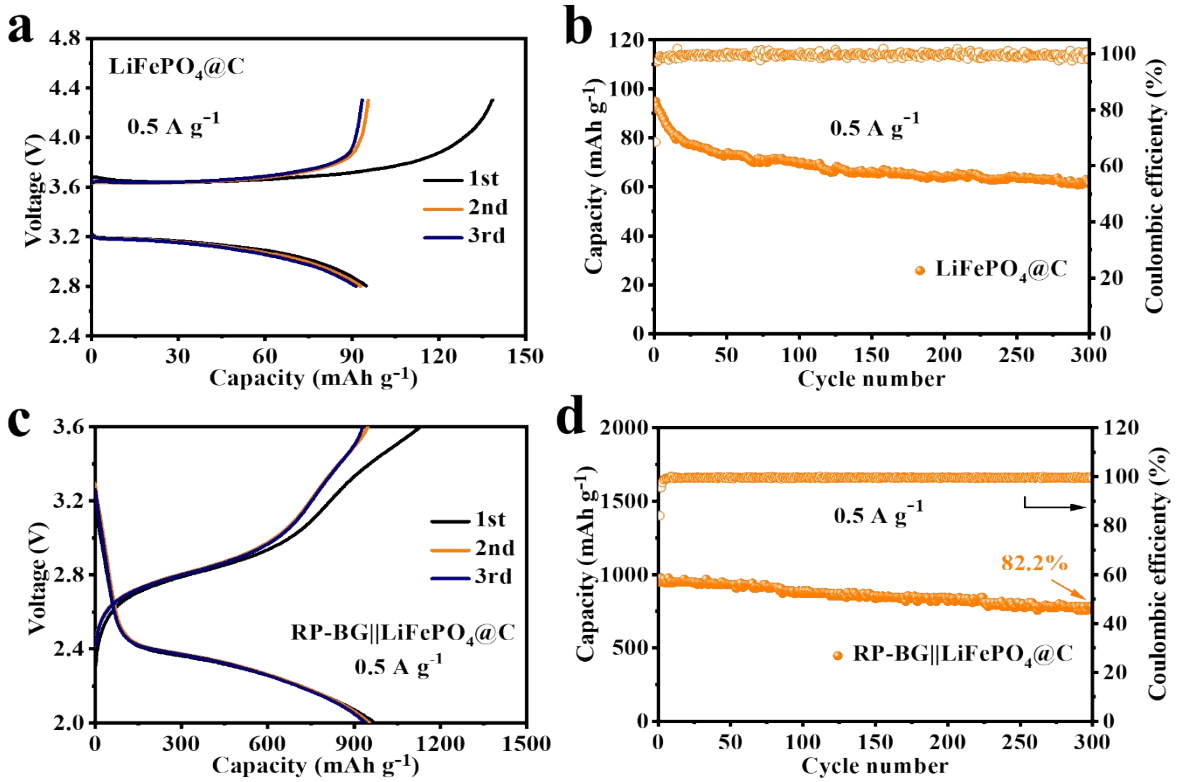

Figure S17. (a) Charge-discharge profiles for the first three scans and (b) cycle performance of $LiFePO_4$@C at 0.5 A g^{-1}. (c) Charge-discharge profiles of RP-BG||$LiFePO_4$@C full cells for the first three scans and (d) cycle performance of BG||$LiFePO_4$@C at 0.5 A g^{-1}.

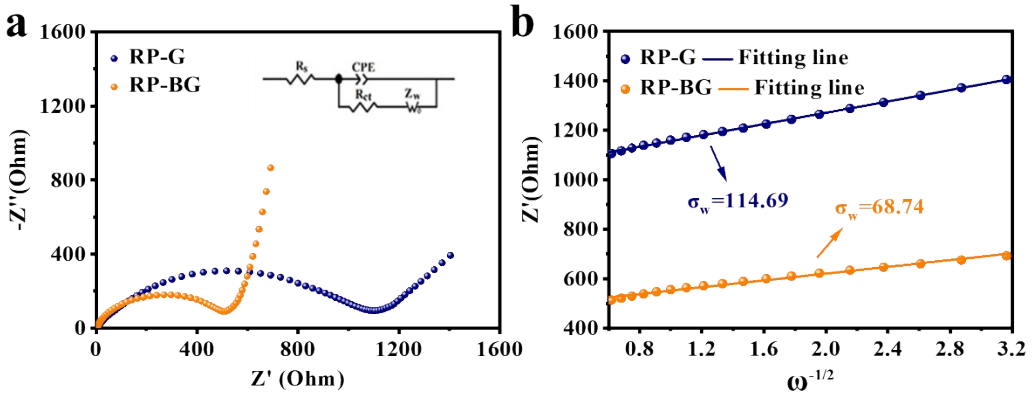

Figure S18. (a) Electrochemical impedance spectra of RP-G and RP-BG (the inset is the corresponding equivalent circuit). (b) The real part of the impedance (Z′) versus the reciprocal square root of the angular frequency ($\omega^{-1/2}$) in the low frequency region.

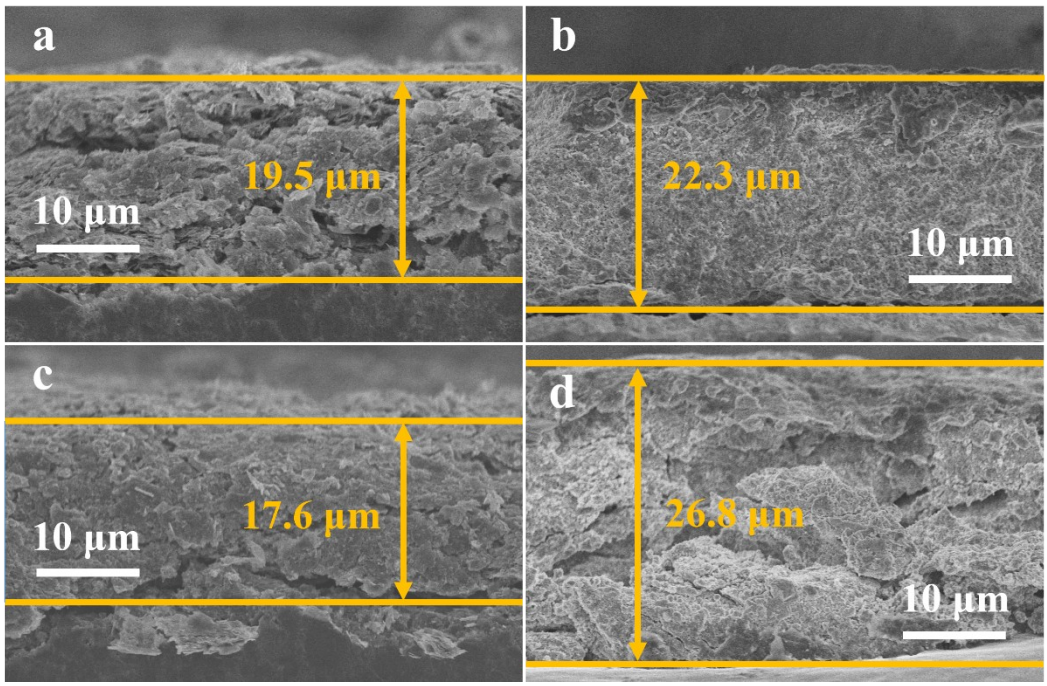

Figure S19. The cross-sectional SEM images of (a-b) RP-BG and (c-d) RP-G electrodes before and after 1000 cycles at 10.0 A g^{-1}.

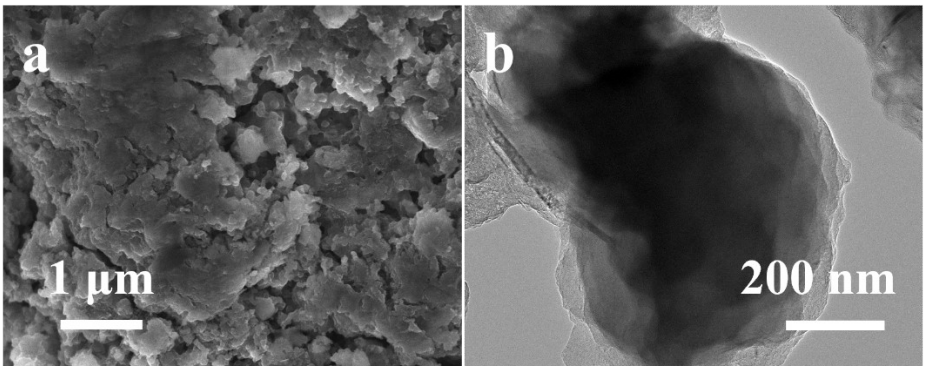

Figure S20. (a) SEM and (b) TEM of RP-G electrode after 1000 cycles at 10.0 A g^{-1}.

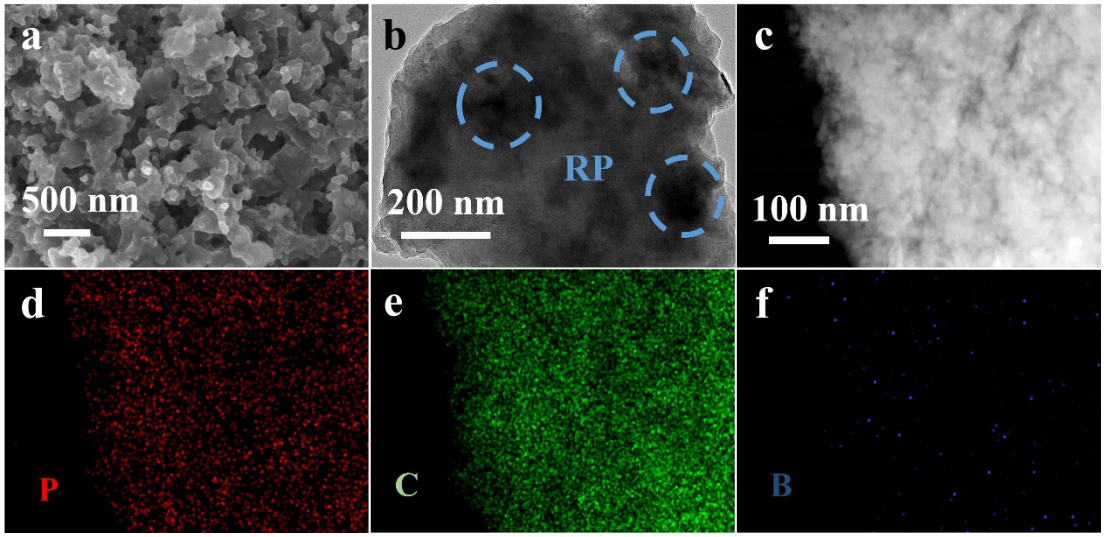

Figure S21. (a) SEM, (b) TEM and (c-f) EDS mapping of RP-BG electrode after 1000 cycles at 10.0 A g^{-1}.

Table S2. Bond lengths of B−C bonds in four different boron doping types

B types	BC_3	BC_2O	BCO_2	B_4C
bond lengths	1.49 Å	1.48 Å	1.49 Å	1.66 Å

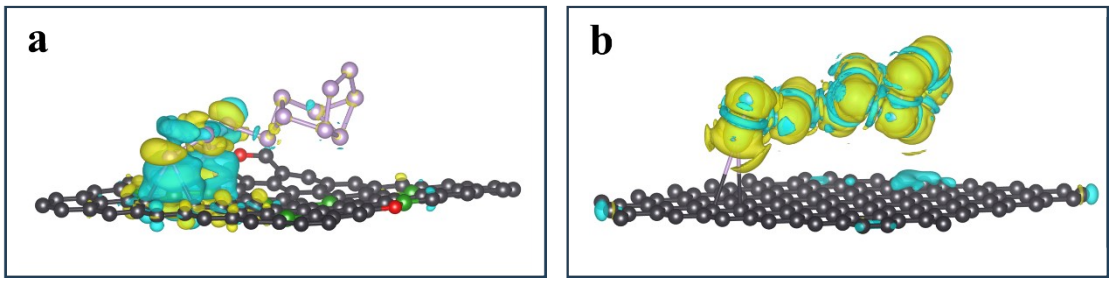

Figure S22. The charge density difference maps of (a) RP-BG and (b) RP-G, the yellow and cyan regions represent the isosurfaces of electron accumulation and depletion, respectively.

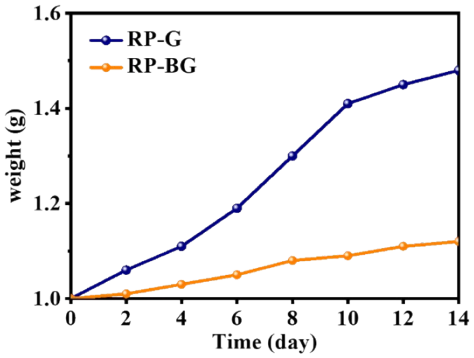

Figure S23. The mass change of RP-BG and RP-G powder during exposure in air.